ARTICLE

Constructing Sub 10 nm Scale Interfused TiO$_2$/SiO$_x$ Bicontinuous Hybrid with Mutual-Stabilizing Effect for Lithium Storage

Ruohan Yu, Yexin Pan, Yihang Liu, Liang Zhou,* Dongyuan Zhao, Jinsong Wu,* and Liqiang Mai*

Read Online

ACCESS | Metrics & More | Article Recommendations | Supporting Information

ABSTRACT: TiO$_2$ has been considered as a promising intercalation lithium-ion-battery (LIB) anode material owing to its robust cyclability. However, it suffers from low capacity. Herein, we construct a sub 10 nm scale interfused TiO$_2$/SiO$_x$ hybrid with a bicontinuous structure, in which bridged TiO$_2$ nanoparticles (over 80 wt %) are densely packed within a wormlike SiO$_x$ network, through the simple oxidation of MAX Ti$_3$SiC$_2$ ceramic. State-of-the-art *in situ* microscopy characterization unravels a "mutual-stabilizing" effect from the interfused TiO$_2$/SiO$_x$ hybrid upon lithiation. That is to say, the two interpenetrated active components restrain the volume expansion of each other with the stress being relieved through abundant interfaces. Meanwhile, the stress generated from one phase functioned as the compressive force on the other phase and vice versa, offsetting the overall volume effect and synergistically reinforcing the structure integrity. Benefiting from the "mutual-stabilizing" effect, the TiO$_2$/SiO$_x$ composite manifests a high and stable specific capacity (∼671 mAh g^{-1} after 580 cycles at 0.1 A g^{-1}) with a low volume expansion of ∼14% even in an extended potential window of 0.01−3.0 V (vs Li$^+$/Li). The concept of mutual-stabilizing effect, in principle, applies to a wide class of interfused bicontinuous hybrids, providing insight into the design of LIB anode materials with high capacity and longevity.

KEYWORDS: *bicontinuous structure, mutual stabilizing, 3D tomography, in situ STEM, titanium dioxide, silicon oxide*
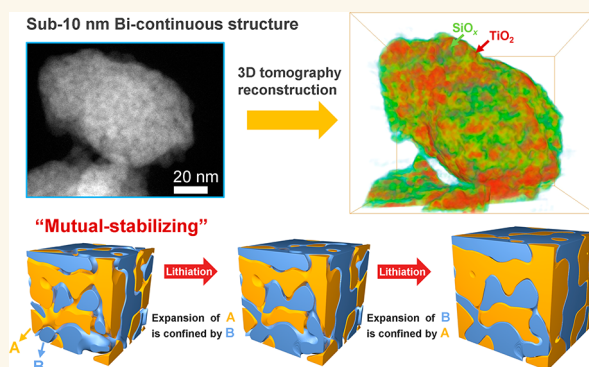
INTRODUCTION

Lithium-ion batteries (LIBs) are currently employed in various applications, from portable electronics to new energy vehicles as well as stationary energy storage. The emerging applications necessitate an evolution in LIB technology and the development of more advanced LIBs with higher energy/power density. The key to achieving this goal lies in the design of advanced electrode materials.[1,2]

Among the various anode candidates, titanium dioxide (TiO$_2$) has been regarded as a potential one due to its high mechanical stability with a slight volume change (∼4%).[3−5] Moreover, the high ionic conductivity can contribute to good performance at high rates.[6,7] However, the high working plateau (∼1.7 V vs Li$^+$/Li) and limited theoretical capacity (∼335 mAh g^{-1}) have hindered its further application. The majority of previous studies have targeted the electrochemical performance in a narrow potential window of 1.0−3.0 V to gain extra structural stability at the price of sacrificing the capacity.[8,9] Thus, extending the electrochemical window from 1.0−3.0 to 0.01−3.0 V for higher capacity would be rewarding

in spite of the accompanying challenges on structural durability, setting a higher standard in structure design.[10]

Compositing the TiO$_2$ with a second phase with a high theoretical capacity can also lead to improved capacity. In this circumstance, silicon oxide (SiO$_x$) stands out for its high capacity, low working voltage, and intrinsic Li conductivity from *in situ* generated Li$_2$O and lithium silicates.[11−13] Nevertheless, the promising property is not free from drawbacks since the lithiation of SiO$_x$ through a conversion-alloying reaction involves a drastic volume effect, pulverization, and accumulated stress in the particle, bringing quick capacity fading.[14−17] It would be ideal that the advantages of the high capacity of SiO$_x$ and stability of TiO$_2$ could compensate for
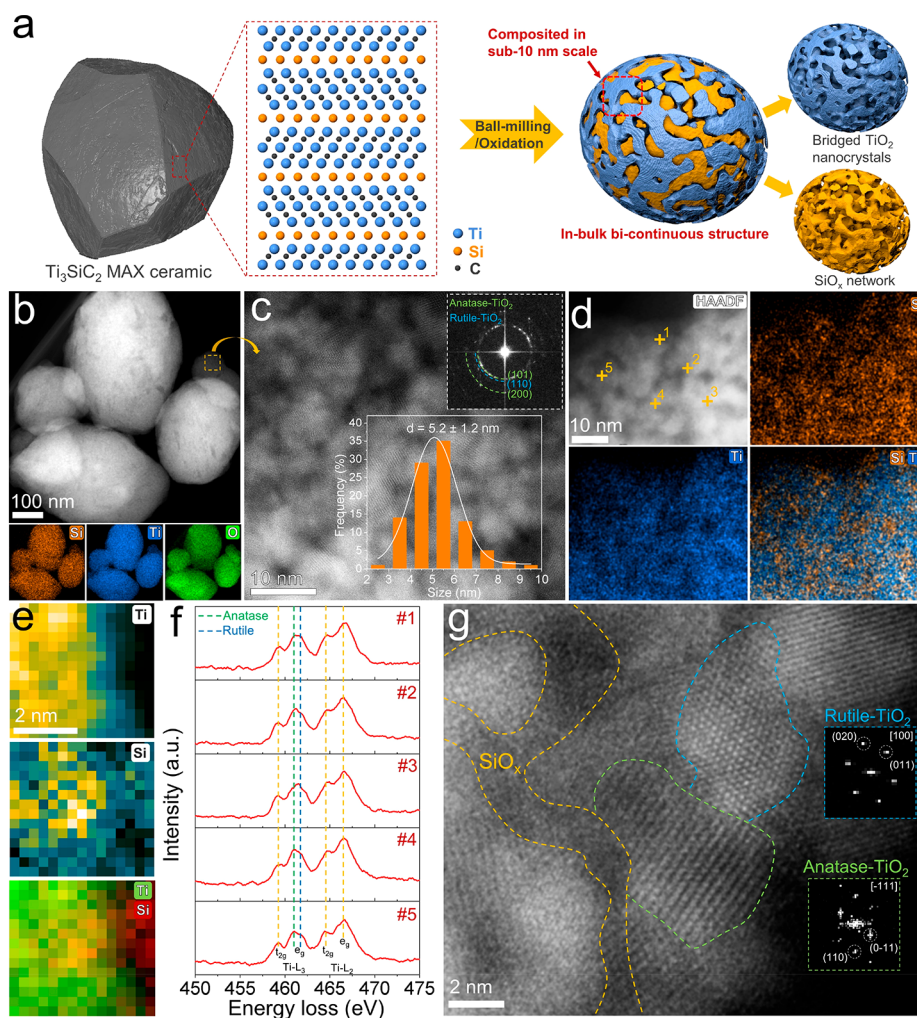
Figure 1. Structural design and electron microscopy characterization of the TiO₂/SiOₓ hybrid: (a) schematic illustration for the construction of the TiO₂/SiOₓ hybrid; (b) HAADF-STEM and corresponding EDX mapping images; (c) high-resolution STEM image with corresponding FFT image and the TiO₂ grain size distribution; (d) HAADF-STEM and corresponding EDX mapping images at high resolution; (e) EELS mappings of Ti, Si, and color mix image; (f) EELS of Ti L edge from five representative points as marked in (d); (g) high-resolution STEM images and corresponding FFT images (inset) converted from the areas marked by blue and green dashed lines.

each other through rational structure design, giving an anode material with both high capacity and longevity.[18−21]

In this work, a sub 10 nm interfused TiO₂/SiOₓ hybrid with a bicontinuous structure, in which bridged heterogeneous TiO₂ nanoparticles (over 80 wt %) are densely packed within a wormlike SiOₓ network, is synthesized through a simple oxidation process of MAX Ti₃SiC₂ ceramic, utilizing its natural atomic Ti/Si dispersion. When it is applied as the LIB anode material, the TiO₂/SiOₓ hybrid exhibits a "mutual-stabilizing" behavior, in which two close-packed components would spatially confine and buffer each other's volume effect, relieving the stress through abundant interfaces during lithiation. As a result, the TiO₂/SiOₓ composite demonstrates a low volume change of ∼14% in an expanded electrochemical window of 0.01−3.0 V and manifests robust structural integrity, high electrochemical activity, and prolonged cyclability (∼671 mAh g⁻¹ for 580 cycles at 0.1 A g⁻¹). This work presents a rational structure design with an unraveled structure−property correlation, providing insights into the development of next-generation LIB anode materials with high capacity and longevity.

RESULTS AND DISCUSSION

Structural Design and Electron Microscopy Characterization. The sub 10 nm interfused bicontinuous TiO₂/SiOₓ hybrid is constructed through ball-milling of MAX Ti₃SiC₂ ceramic followed by calcination (Figure 1a), which is simple, low-cost, and scalable. The ball-milling process would transform the micrometer-sized sharp flakes (Figure S1a) into sub-micrometer-sized ellipsoid-shaped particles (Figure S1b). Plenty of cracks appear (Figure S1c) after ball milling, which is beneficial for the subsequent uniform oxidation, as reflected by the thermogravimetric (TG) curves (Figure S2). The reduced particle size and enriched defects after ball milling are also reflected in the broadening of X-ray diffraction (XRD, Figure S1d) peaks. The formation of the sub 10 nm dimensional size of TiO₂ and SiOₓ is believed to originate from the naturally well-defined Si/Ti atomic dispersion in the MAX phase Ti₃SiC₂ precursor and the two-phase mutual confining effect: the oxidation during high-temperature annealing first removes the carbon and leads to the nucleation of TiO₂ and SiOₓ. Then, the high-temperature calcination-induced surface energy reduction would lead to pore ejection as well as the attachment of TiO₂ and SiOₓ, forming a dense and bicontinuous structure.
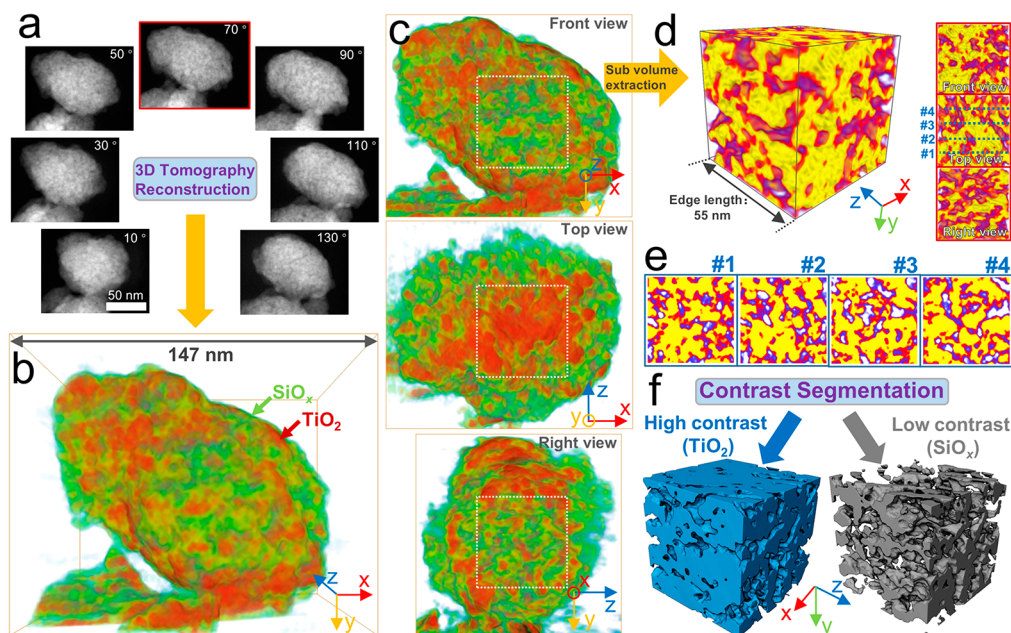
Figure 2. Illustration of the sub 10 nm bicontinuous structure by 3D tomography reconstruction: (a) representative STEM-HAADF images of an individual TiO_2/SiO_x hybrid particle at different rotation angles; (b, c) reconstructed TiO_2/SiO_x hybrid particle (b) and corresponding front, top, and right views (c); (d) extracted volume in a cube with an edge length of 55 nm from the labeled white dashed line area in (c) (front, top, and right views are inset on the right); (e) representative orthoslices (*xy* planes, perpendicular to the *z* axis at 11, 22, 33, and 44 nm) marked by the blue dashe lines in (d); (f) volumes from segmentation by contrast corresponding to TiO_2 (blue) and SiO_x (gray).

The hence enabled "mutual spatial confinement" in the two-phase composited continuous structure has restrained the further growth size: the growth of TiO_2 has been prohibited by the closely packed SiO_x and vice versa.

Aiming to unravel the microstructure, electron microscopy characterization based on a double aberration correction transmission electron microscope (TEM) has been carried out. The low-magnification high-angle annular dark-field (HAADF) scanning transmission electron microscope (STEM) image and corresponding energy dispersive X-ray spectroscopy (EDX) mappings as shown in Figure 1b present a dense structure with an ellipsoid shape and fine-grained texture, while Si, Ti, and O elements are uniformly distributed within the particle. The pore structure of the as-prepared samples has been examined by N_2 sorption (Figure S3). The TiO_2/SiO_x hybrid shows a low surface area of 5.75 m² g⁻¹, indicative of a dense structure, which is beneficial for the formation of a stable solid electrolyte interphase (SEI) layer. The bicontinuous structure is revealed by higher-resolution HAADF images (Figure 1c), which is magnified from the marked area in Figure 1b. The nanoparticles with bright contrast bridge with each other to form a continuous structure. Also, crystal lattices are observed on the bright nanoparticles with distinct lattice distances corresponding to the (101)/ (200) planes of anatase TiO_2 and the (110) planes of rutile TiO_2, which are marked on the corresponding fast Fourier transform (FFT, inset in Figure 1c) pattern by green and blue dashed lines, respectively. In order to illustrate the sub 10 nm interfused bicontinuous structure, a higher-resolution HAADF STEM-EDX characterization is carried out. As presented in Figure 1d, the Si and Ti signals show an inhomogeneous distribution, where the Si signal distribution is well matched with the dark contrast area in the HAADF images while the Ti signal distribution is associated with the bright area, which agrees well with the mass contrast, since the atomic number of

Ti (22) is higher than that of Si (14). Also, the Si/Ti color mix image shows an obvious wormlike Si signal distribution within the Ti signal distribution, indicative of a bicontinuous structure with abundant curvatures at the contact interface, which is beneficial for relieving the stress.

To further determine the chemical composition of the TiO_2/SiO_x hybrid, electron energy-loss spectroscopy (EELS) is carried out for its advantage in chemical bonding analysis with high spatial and energy resolution. It is observed that the Si and Ti elements are inhomogeneously distributed, and an Si signal with a size of ∼2 nm is closely surrounded by an Ti signal. Such an observation matches well with the size of SiO_x observed in Figure 1e. The heterogeneous nature of TiO_2 is further analyzed by an EELS point scan (Figure 1f). Five representative points are selected from the labeled points in Figure 1d. All of the spectra have a similar shape. They are composed of two major contributions (the L_3 and L_2 edges) separated by the 2p core-hole spin−orbit coupling of ∼5 eV. L_3 and L_2 edges are both further divided into two subedges through strong crystal-field splitting arising from the neighboring O atoms. The e_g feature of the Ti L_3 edge shows a broader asymmetric splitting into two peaks marked by green and blue dashed lines. Their intensity ratios provide information on symmetric variation in the $[TiO_6]$ octahedra. For both anatase and rutile, they show double peaks in the L_3 edge at 461.0 and 461.7 eV but with obvious differences in relative intensity. In anatase, the peak at 461.0 eV is more intense, while in rutile, the peak at 461.7 eV is more intense.[22,23] It is observed that all spectra show the coexistence of both phases, except that the spectra from points 2 and 3 show major anatase and rutile phase distributions, respectively, indicative of the uniform and dense spread of anatase/rutile heterojunctions in the bridged TiO_2 nanoparticles. According to previous studies, such densely distributed heterojunctions of
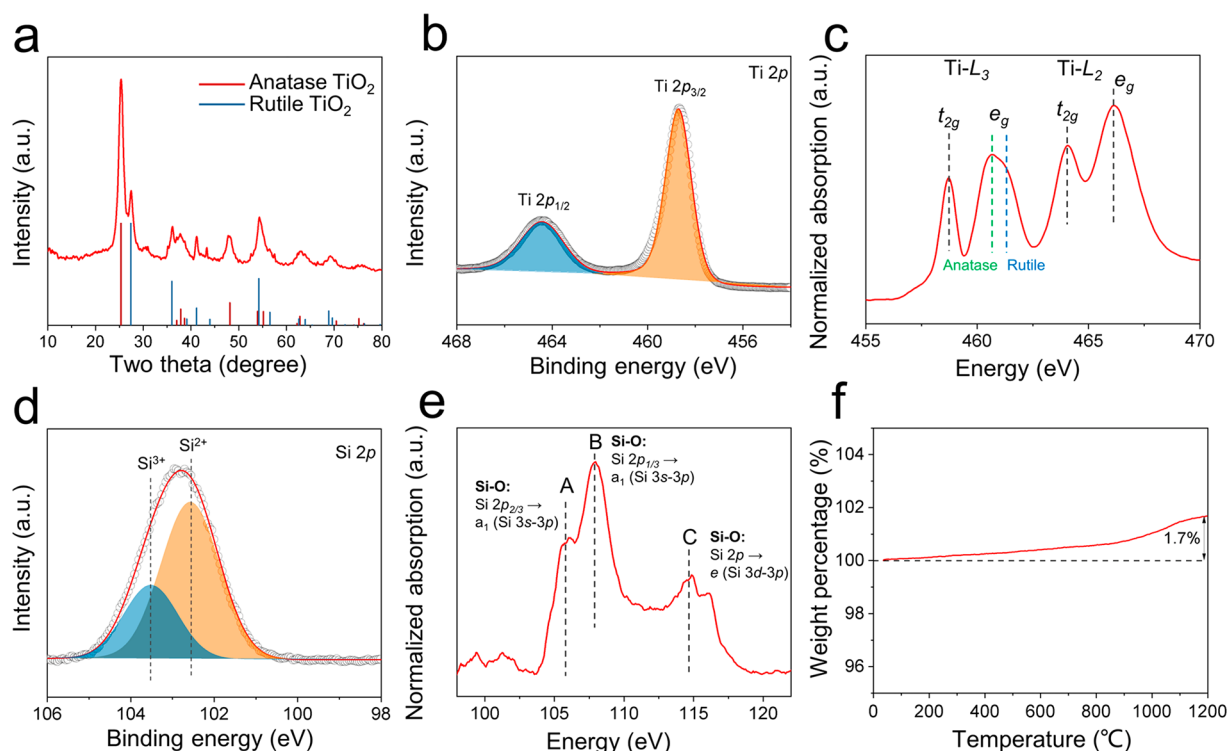
Figure 3. Chemical composition and environment characterization of TiO_2/SiO_x hybrid: (a) XRD pattern; (b) Ti 2p XPS; (c) Ti 2p XANES; (d) Si 2p XPS; (e) Si 2p XANES; (f) TG curve.

anatase and rutile phases could effectively lower the Li^+ migration barrier.[24−26]

The amorphous distinction of SiO_x and heterogeneous nature of TiO_2 are further unraveled by atomic-resolution HAADF STEM (Figure 1g). The SiO_x area with weakened contrast marked by orange dashed lines exhibits a typical amorphous distinction. For TiO_2, the selected area indicated by green dashed lines is determined to be the [−111] orientation of the anatase phase, while the area in blue dashed lines is determined to be the [100] orientation of a rutile phase, which further provides evidence for the heterojunction in the heterogeneous TiO_2.

To further prove the sub 10 nm bicontinuous structure, three-dimensional (3D) tomography reconstruction is carried out. 70 STEM-HAADF images for tomography reconstruction were collected by a 2° interval, over preferably 140° (Figure 2a, Video 1). The reconstructed particle placed at a front view is shown in Figure 2b, which resembles in shape the HAADF image taken at 70°, marked with a red frame in Figure 2a. The length (x axis), width (z axis), and height (y axis) of the bonding box are 147, 125, and 121 nm, respectively. The contrast of volume is presented in Physics color mode, where the volume in red/green represents relatively high/low HAADF contrast, corresponding to TiO_2/SiO_x components, respectively. The front-, top-, and right-view images are shown in Figure 2c. Since SiO_x has a relatively low contrast, it can be filtered and removed by adjusting the contrast range for a better visual presentation of the solo TiO_2 phase (Figure S4a), which is more obvious when the contrast is altered to Temperature (Figure S4b; the volume in yellow/purple represents relatively high/low HAADF contrast). The rotation, filtering, and orthoslicing process of the reconstructed particle are presented in both Physics and Temperature color modes for a better view (Video 2).

To further confirm the bicontinuous structure, a subvolume cube with an edge length of 55 nm is extracted from the white dashed line marked area in Figure 2c. The contrast is converted to Temperature for a better visualization of the inner structure (Video 3). Both the surface (Figure 2d) from views in different directions and the inner structure (Figure 2e and Figure S4c,d) from orthoslices are identified to be bicontinuous. Furthermore, a segmentation is conducted to separate the high contrast volume (represents TiO_2) and low contrast volume (represents SiO_x) according to the STEM-HAADF contrast. Both volumes extracted from contrast segmentation are proven to be continuous (Video 4), providing a direct evidence for the sub 10 nm bicontinuous structure.

From the above characterizations, it is clear that due to the atomic mixing of Ti and Si in the MAX phase precursor, the thermodynamically metastable phases (including amorphous SiO_x and anatase TiO_2 at sub 10 nm scale) are stabilized in the form of an interpenetrating, bicontinuous, and densely packed structure. The mutual-stabilizing effect due to nanoscale confinement could play an important role in the structural evolution from the MAX phase precursor to the final formation of the sub 10 nm interfused bicontinuous TiO_2/SiO_x hybrid.

Chemical Composition and Environment Characterization. Aiming to better understand the chemical composition and environment of the TiO_2/SiO_x hybrid, XRD, X-ray photoelectron spectroscopy (XPS), X-ray absorption near edge spectroscopy (XANES), and TG analysis were carried out. The XRD pattern (Figure 3a) exhibits a number of diffractions which can be well-indexed to anatase and rutile TiO_2, as indicated by red and blue lines, respectively. With an increase in calcination temperature, the crystallization degree increases and the anatase/rutile ratio decreases (Figure S5). The chemical composition of TiO_2 is further illustrated by XPS
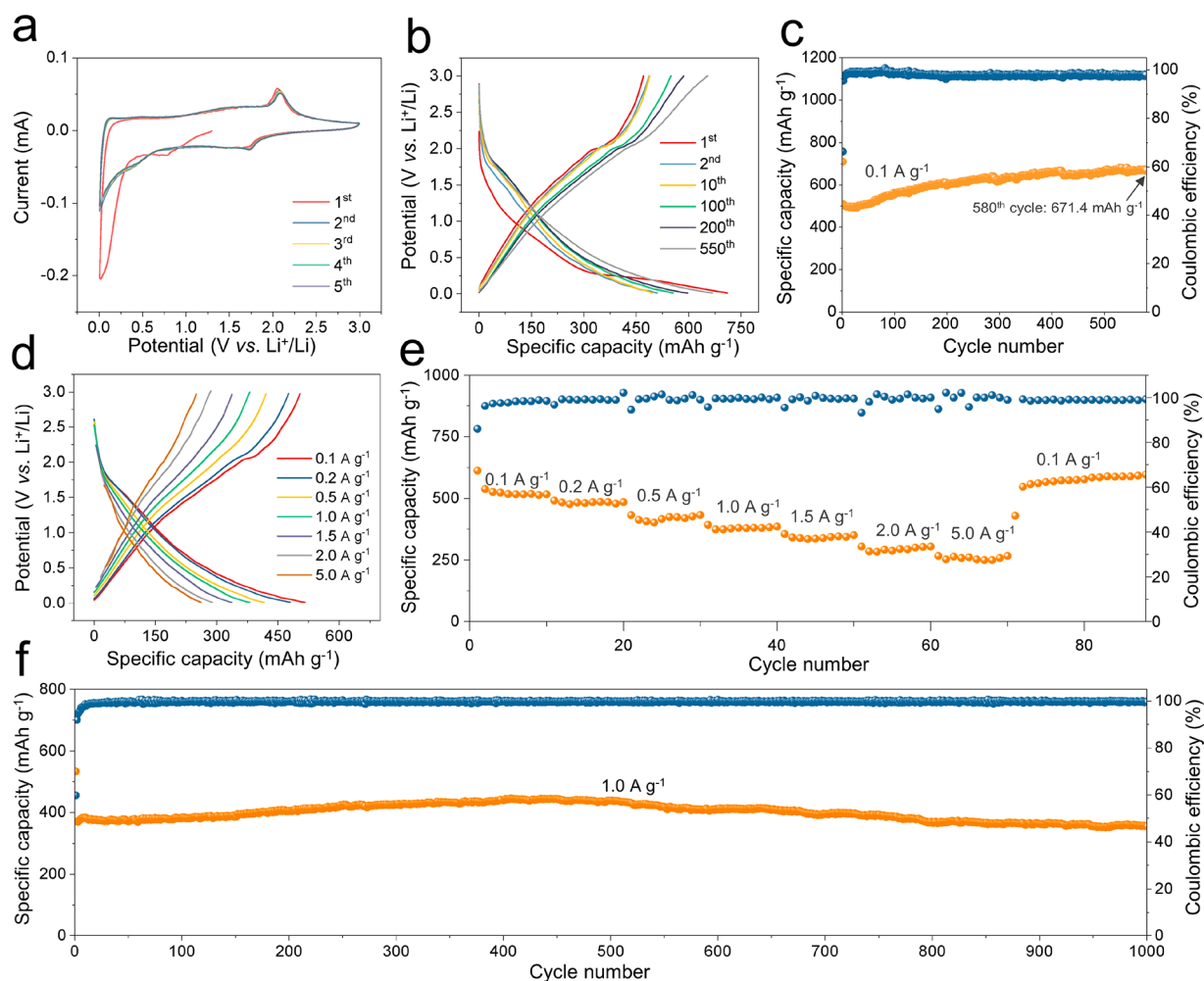
Figure 4. Electrochemical performance of the TiO$_2$/SiO$_x$ hybrid: (a) CV curves of the TiO$_2$/SiO$_x$ hybrid at 0.1 mV s^{-1}; (b, c) galvanostatic charge−discharge profiles and cycling performance of the TiO$_2$/SiO$_x$ hybrid at 0.1 A g^{-1}, respectively; (d, e) representative charge/discharge curves and rate performance of the TiO$_2$/SiO$_x$ hybrid, respectively; (f) cycling performance at 1.0 A g^{-1}.

and XANES. For Ti 2p XPS (Figure 3b), the peaks at 464.4 and 458.7 eV can be well assigned to the 2p$_{1/2}$ and 2p$_{3/2}$ components of Ti(IV). In the XANES results (Figure 3c), the crystal field splitting in [TiO$_6$] octahedra results in the splitting of 3d orbitals into two sub levels, t$_{2g}$ and e$_g$. Similar to EELS (Figure 1f), the peaks at 460.7 and 461.2 eV in e$_g$ of the L$_3$ edge could be used to distinguish anatase and rutile phases: the anatase phase shows a more intense peak at 460.7 eV, while the rutile phase shows a more intense peak at 461.2 eV. Thus, the broad e$_g$ peak in the TiO$_2$/SiO$_x$ hybrid suggests the coexistence of two crystal phases. According to the higher intensity of anatase peaks in both XANES and XRD, the anatase phase should account for the major component in the heterogeneous TiO$_2$. For SiO$_x$, the Si 2p XPS spectrum (Figure 3d) presents a main peak at 102.8 eV, which can be further deconvoluted into two components at 103.5 and 102.5 eV[27] from Si^{3+} (30.2%) and Si^{2+} (69.8%), indicative of a Si valence of ~2.3 ($x \approx 1.15$) and the nondisproportionation feature of SiO$_x$. The peak A in the L edge XANES corresponds to the transition of Si 2p electrons to the antibonding 3s-like a$_1$ state in the Si−O bonding system. The splitting of this peak by ~0.6 eV is ascribed to the spin−orbital interaction of Si 2p orbitals. Peak B is assigned to the transition of Si 2p electrons to the t$_2$ state. For peak C, in the T_d crystal field, the Si 3d

orbitals are split into e and t$_2$ states, the e states are favored in energy over t$_2$, and peak C is assigned to a transition to the e states. No obvious peaks located at 99−100 eV are found, indicating little disproportionation even after the high-temperature annealing process. The nondisproportionation feature of SiO$_x$ is believed to be from the spatial confinement from the close-packed TiO$_2$, which matches well with the XPS results. The TG curve in Figure 3f shows a mild increasing trend, which could be assigned to the oxidation of SiO$_x$, suggesting complete removal of carbon from MAX Ti$_3$SiC$_2$ as well as the unsaturated coordination of Si. Thus, from the XPS, XANES, TG, and atomic resolution STEM measurements, the nature of SiO$_x$ could be revealed as a Si−O bond dominated amorphous structure.

Electrochemical Performances. Cyclic voltammetry (CV) profiles of the TiO$_2$/SiO$_x$ hybrid are presented in Figure 4a. The sharp redox peaks at 1.7/2.0 V (vs Li$^+$/Li) can be attributed to the electrochemical Li$^+$ insertion/extraction of TiO$_2$. The reductive decomposition of electrolyte for SEI formation[28] leads to a small cathodic peak at 0.75 V in the first discharge process, indicative of a thin SEI due to the minimized surface area. The broad cathodic peak at 0−0.5 V corresponds to the conversion-alloying reactions of SiO$_x$. The conversion reaction process lies at upper potential (>0.4 V)
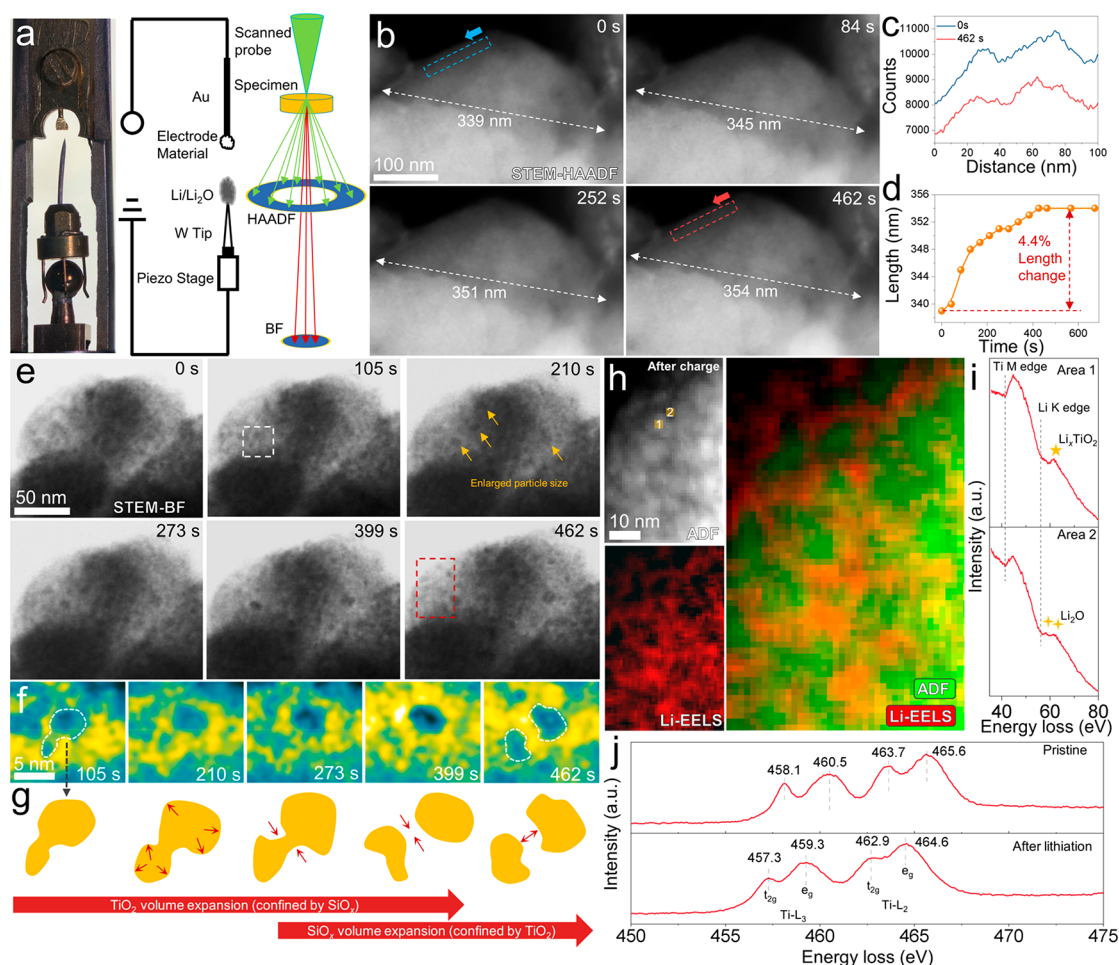
Figure 5. *In situ* STEM/EELS characterization of the TiO$_2$/SiO$_x$ hybrid on lithiation: (a) schematic illustration of *in situ* STEM characterization; (b, c) time-lapse HAADF-STEM images of the TiO$_2$/SiO$_x$ hybrid during first lithiation and intensity profiles from the marked areas, respectively; (d) length change of the TiO$_2$/SiO$_x$ hybrid particle; (e) time-lapse BF-STEM images of the TiO$_2$/SiO$_x$ hybrid during the first lithiation; (f) contrast converted images from the selected area (white dashed line rectangle in (e)); (g) morphology evolution of the marked place in (f); (h) ADF image of the TiO$_2$/SiO$_x$ hybrid (upper left), Li K edge EELS signal mapping (lower left) and color mix image of ADF and Li EELS mapping (right) after *in situ* lithiation; (i) EELS of Ti M edge and Li K edge from representative places as marked in the ADF image in (h); (j) EELS of Ti L edge of TiO$_2$/SiO$_x$ hybrid before and after *in situ* lithiation.

with the products of Li$_2$O, lithium silicates,[29] and Si, while the alloying reaction (Si + x Li → Li$_x$Si) happens at lower potential (<0.4 V). The broad anodic peak at 0.1−1.5 V corresponds to the dealloying processes of Li$_x$Si. In subsequent cycles, a new broadened cathodic peak appears at ∼0.4 V with the activation of the material, which corresponds to the relithiation of Si. The slight shift to higher potential is caused by the nanosizing of active components.[15,30] The oxidation peak for subsequent cycles overlaps with that of the first cycle.

To evaluate the Li$^+$ storage capabilities of the TiO$_2$/SiO$_x$ hybrid under deep charge/discharge conditions, a low-current-density (0.1 A g^{-1}) cycling was first carried out (Figure 4b,c). Interestingly, the discharge capacity experiences a gradual increase from 508.9 to 671.4 mAh g^{-1} from the 2nd cycle to the 580th cycle, showing an outstanding deep charge/discharge cyclability. The capacity increase can be ascribed to the gradually formed defects in the TiO$_2$/SiO$_x$ interface during cycling, which exposes extra lithium storage sites. The first discharge and charge capacities are 709.8 and 470.6 mAh g^{-1}, leading to an initial Coulombic efficiency (ICE) of 66.3%. The initial capacity loss might be from the formation of an SEI as well as irreversible products (Li$_2$O and lithium silicate) from

the conversion reaction of SiO$_x$, which could be tackled with prelithiation strategies.[31−34] To understand the electrochemical activation process, *in situ* electrochemical impedance spectra (EIS; Figure S6) are collected at 0.1 A g^{-1} for the cell before cycling and after 1, 5, 10, 25, and 50 cycles. The charge transfer resistance reflected from the semicircle shows a rapid decrease from 173 to 55 Ω at the discharge state after 1 cycle and remains almost stable in the following cycles. The improved charge transfer is associated with the delithiated products of TiO$_2$ and SiO$_x$,[10,35−37] which provide fast Li$^+$ diffusion kinetics.

Figure 4d,e shows the rate performance and corresponding representative charge/discharge profiles at different current densities. At 0.1 A g^{-1}, the discharge capacity reaches 513.5 mAh g^{-1}. With an increase in current density, the discharge capacity decreases to 491.1 mAh g^{-1} at 0.2 A g^{-1}, 432.1 mAh g^{-1} at 0.5 A g^{-1}, 392.6 mAh g^{-1} at 1.0 A g^{-1}, 355.3 mAh g^{-1} at 1.5 A g^{-1}, 304.5 mAh g^{-1} at 2.0 A g^{-1}, and 266.6 mAh g^{-1} at 5.0 A g^{-1}, with 95.6%, 84.1%, 76.5%, 69.1%, and 51.9% capacity retention, respectively. The good fast-charging capability is believed to be due to the structure design. The capacity restores to 546.9 mAh g^{-1} when the current density is

again reduced to 0.1 A g^{-1}. At a current density of 1.0 A g^{-1}, the TiO$_2$/SiO$_x$ hybrid delivers a discharge capacity of 370.7 mAh g^{-1} at the second cycle with a mild transition to 355.3 mAh g^{-1} at the 1000th cycle. The capacity retention reaches 95.8% (Figure 4f), demonstrating an excellent long-term cycling performance. A comparison of TiO$_2$/SiO$_x$ hybrids prepared at various calcination temperatures (600, 700, 800, and 900 °C) is presented in Figure S7, and the sample prepared at 800 °C shows the best cycling stability and capacity, indicative of an optimized structure.

To further illustrate the advantage of the sub 10 nm scale bicontinuously interfused structure, three contrasting samples, including (1) TiO$_2$ nanoparticles (Sample 1), (2) mechanically mixed TiO$_2$ and Si (Sample 2), and (3) mechanically mixed TiO$_2$ and SiO$_x$ (Sample 3; the Ti/Si mole ratio is 3:1, the same as that of the TiO$_2$/SiO$_x$ hybrid), are prepared and tested. In sample 1, the anatase TiO$_2$ nanoparticles with sizes of ~10−20 nm are bridged (Figure S8), while in the mechanically mixed TiO$_2$/Si (Sample 2) and TiO$_2$/SiO$_x$ (Sample 3), Si and SiO$_x$ nanoparticles (with size ~100 nm) dispersed within the TiO$_2$ particles can be clearly seen (Figures S9 and S10). The three contrasting samples show poor cycling, capacity, and rate performances (Figure S11). In comparison with previous works on TiO$_2$-based composite anode materials (Table S1 and Figure S12), the obtained TiO$_2$/SiO$_x$ hybrid in this study stands out in cycling performance as well as rate performance.

To assess the validity of the TiO$_2$/SiO$_x$ hybrid, full cells were assembled using the TiO$_2$/SiO$_x$ hybrid as the anode and commercial LiFePO$_4$ (LFP) as the cathode. Considering the low ICE of the TiO$_2$/SiO$_x$ hybrid, the anodes were prelithiated in half-cells. The capacity of the TiO$_2$/SiO$_x$‖LFP full cell is determined based on the mass of LFP. The representative charge−discharge curve and cycling performance at 0.5 C are shown in Figure S13. The TiO$_2$/SiO$_x$‖LFP full cell manifests a specific discharge capacity of 127.7 mAh g^{-1} at 0.5 C and maintains 110.8 mAh g^{-1} after 100 cycles (86.8% capacity retention), proving its cycling stability under practical working conditions.

Dynamic Structure Evolution of the TiO$_2$/SiO$_x$ Hybrid during Lithiation. *In situ* STEM is employed for characterizing the dynamic structural evolution of the sub 10 nm interfused bicontinuous TiO$_2$/SiO$_x$ hybrid during lithiation. Figure 5a shows a photo and schematic illustration of the micronanobattery configuration for *in situ* STEM tests. A micronanobattery is built inside the transmission electron microscope, with the TiO$_2$/SiO$_x$ hybrid on the gold pad as the cathode and lithium metal attached to the surface of the tungsten needle as the anode. Li$_2$O from the surface oxidation of lithium metal serves as the solid electrolyte. Compared to the conventional *in situ* TEM mode where images are formed by the objective lens and recorded by a charge-coupled device, *in situ* STEM images are recorded by both a HAADF and a bright-field (BF) detector. The *in situ* STEM allows us to simultaneously collect dark-field and bright-field images and utilize their combined advantages, although it has lower temporal resolution than conventional *in situ* TEM.

A TiO$_2$/SiO$_x$ hybrid particle is picked for *in situ* HAADF-STEM characterization. As disclosed in Figure 5b, when Li$^+$ inserts into the TiO$_2$/SiO$_x$ hybrid, it gradually expands uniformly with no crack or concave/convex formation and maintains its original morphology (Video 5). The intensity profiles collected from the blue and red rectangles in time-lapse images of 0 and 462 s are shown in Figure 5c. The decrease in

HAADF contrast intensity (10−20%) suggests the lowering of the average atomic number contrast (Z-contrast), indicative of the lithium insertion. After discharging for 462 s at the bias of 5 V, the size of the TiO$_2$/SiO$_x$ hybrid expanded gradually from 339 to 354 nm with a length change of ~4.4% (Figure 5d), corresponding to a volume change of ~13.9%.

Considering the high-contrast distinction of the BF-STEM image, a series of higher resolution time-lapse images could be obtained to study the structural evolution of the sub 10 nm interfused TiO$_2$/SiO$_x$ hybrid during lithiation (Figure 5e). Before lithiation, the TiO$_2$/SiO$_x$ hybrid shows a uniform fine-grained texture, where the dark and bright areas are assigned to TiO$_2$ and SiO$_x$, respectively. During lithiation, the TiO$_2$ grains are gradually enlarged with a darkened contrast, as marked by the orange arrows. The enlargement is caused by the lithiation-induced volume effect, while the accompanied darkened contrast can be ascribed to the stress accumulation within the crystal. For SiO$_x$, an enlarged size with bright contrast appears over lithiation, bringing more distinct contrast compared with the TiO$_2$ grains (Video 6). To gain further information on the structural evolution at the nanoscale, a representative place marked by a white rectangle is picked for a magnified view. Due to the higher resolution and better contrast of the BF-STEM image, a clear distinction between TiO$_2$ and SiO$_x$ could be obtained after filtering by a combined method and converting the original grayscale contrast into an aquatic contrast (Figure 5f), where the blue/yellow in aquatic contrast corresponds to the dark/bright contrast in grayscale, respectively. Also, the blue area enclosed by a white dashed line is selected and extracted in Figure 5g for a better view. It is observed that the two TiO$_2$ particles enlarged and darkened mainly from 0 to 399 s, followed by a widened intergranular distance caused by the volume expansion of SiO$_x$ with an obviously brightened contrast mainly from 273 to 462 s, indicative of a consecutive lithiation in the hybrid composed of two active materials with different lithiation potentials.

To further understand the roles of TiO$_2$ and SiO$_x$ in lithium storage, an *in situ* STEM combined with EELS analysis is carried out (Figure 5h−j). Figure 5h shows the annular dark-field (ADF) image with EELS Li mapping image from the area marked by a red rectangle in Figure 5e after *in situ* lithiation. The ADF-STEM image shows that the morphology of the bicontinuously interfused TiO$_2$ (bright area) and SiO$_x$ (dark area) is well-maintained at full lithiation state, proving the good structural integrity. Also, the signal mapping from the Li K edge indicates that the Li signal is mainly distributed in the SiO$_x$ (dark contrast) area, exhibiting a wormlike shape on a sub 10 nm scale with no agglomeration. This result shows that the lithiation of SiO$_x$ under sub 10 nm scale spatial confinement contributes a large amount of lithium storage, and despite its intrinsically large volume effect, the small size of SiO$_x$ is well maintained. To gain insight into the lithiation behavior of the TiO$_2$/SiO$_x$ hybrid, two representative places from ADF images, namely areas 1 and 2, are picked as TiO$_2$-rich and SiO$_x$-rich areas for the Ti M and Li K edge EELS analysis (Figure 5i). EELS from area 1 possesses a much stronger Ti M signal than area 2, implying a significantly higher Ti content. For the Li K edge in area 1, the peak at 61.4 eV could be assigned to Li$_x$TiO$_2$,[38,39] indicating the intercalation of lithium into TiO$_2$, while in area 2, the two peaks at 58.3 and 62.0 eV could be assigned to Li$_2$O,[40−42] which is the lithiation product of SiO$_x$. Both acquired lithiation products could facilitate the
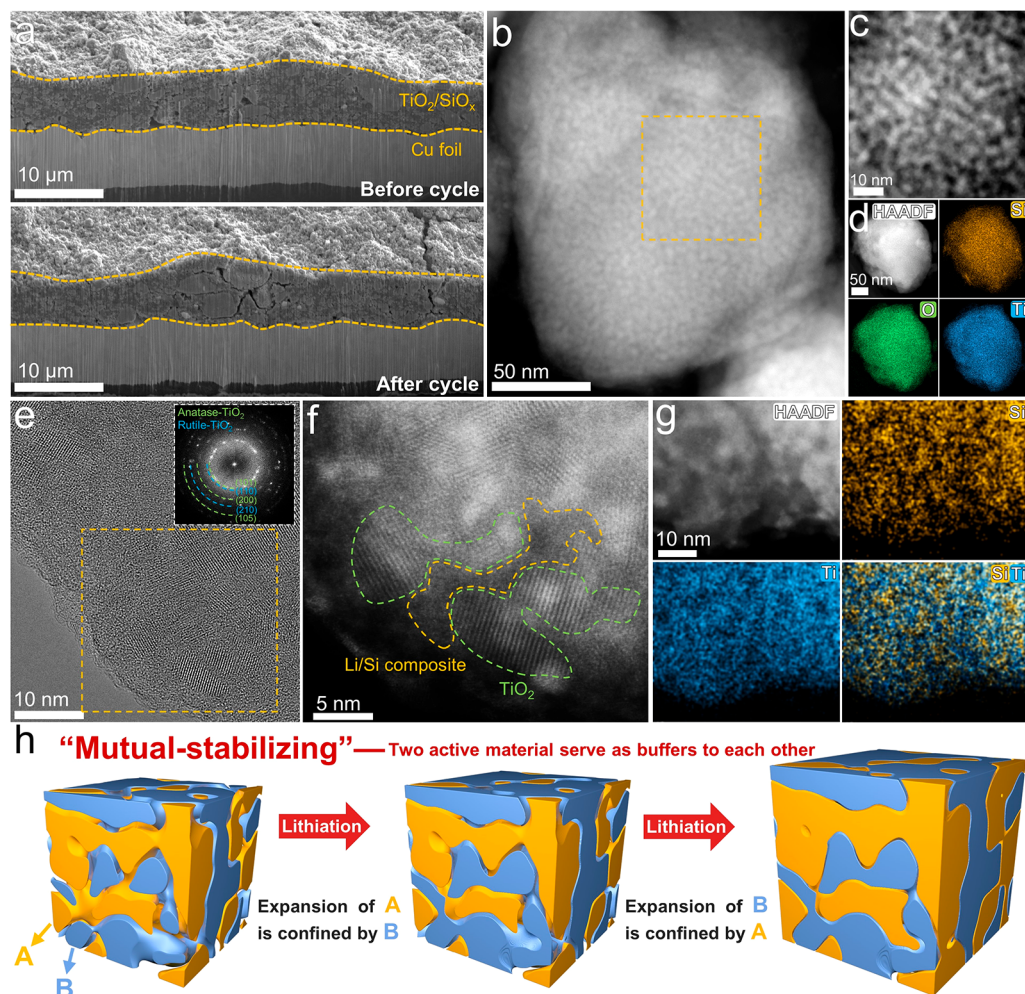
Figure 6. Structural integrity of the TiO_2/SiO_x hybrid and the "mutual-stabilizing" effect: (a) SEM images before and after cycling; (b) HAADF image of the TiO_2/SiO_x hybrid particle after cycling; (c) magnified view from the selected area in (b); (d) HAADF image and corresponding EDX mappings of a TiO_2/SiO_x hybrid particle after cycling; (e) TEM image with corresponding FFT image (inset) after cycling; (f) atomic-scale HAADF image after cycling; (g) HAADF image and corresponding EDX mappings at high resolution after cycling; (h) schematic illustration of the general "mutual-stabilizing" effect of the sub 10 nm scale interfused bicontinuous material during lithiation.

kinetics in the subsequent cycles due to their relatively high lithium ion transfer rate.

Besides the high capacity contributed by spatially confined SiO_x, TiO_2 is also able to contribute a certain capacity. The Ti L edge EELS of the TiO_2/SiO_x hybrid before and after *in situ* lithiation are compared in Figure 5j. Both spectra presented four peaks corresponding to t_{2g} and e_g peaks from Ti $L_{2,3}$. The lithiated TiO_2 largely inherits the t_{2g}/e_g peak splitting in pristine TiO_2, indicative of a well-crystallized lithiation product with $[TiO_6]$ octahedral coordination similar to (but not identical with) those in pristine TiO_2. Beyond the peak splitting, the energy loss position could provide valuable information, since this peak is sensitive to the valence of Ti. After lithiation, the positions of these four energy levels shift to a lower energy region with a value of ~ 1.0 eV, indicating a sufficient reduction from Ti^{4+} to Ti^{3+}, which is consistent with previous reports.[43−46] The distinct fine structures shown here suggest that, beyond the structure integrity, the sub 10 nm bicontinuous hybrid also enabled a sufficient lithiation from TiO_2 to Li_xTiO_2 ($x \approx 1$) by facilitating the lithium storage kinetics, contributing to high capacity.

Structural Integrity and the "Mutual-Stabilizing" Effect. To further illustrate the structural integrity of the

TiO_2/SiO_x hybrid, *ex situ* SEM and TEM characterizations are carried out. Figure 6a shows the cross-sectional SEM images of the TiO_2/SiO_x hybrid electrode before cycling (top) and after 580 cycles (bottom). The cross-sectional views of the two electrodes are almost identical in shape and thickness, except for some cracks appearing after cycling, which is also reflected in the top-view images (Figure S14). The mild electrode-level structural damage can be ascribed to a small volume change of the TiO_2/SiO_x hybrid during (de)lithiation. For the individual particle (Figure 6b,c), it is observed that the fine-grained texture as well as the bicontinuous structure is well-retained even after 580 cycles. Also, the corresponding Si, O, and Ti signals are distributed homogeneously on the particle (Figure 6d). To further investigate the retention of the sub 10 nm interfused bicontinuous structure, high-resolution BF and HAADF images are collected. The BF image (Figure 6e) shows well-crystallized grains with distinct lattice distances for both anatase and rutile TiO_2, which are also reflected in the corresponding FFT pattern. Figure 6f shows the atomic resolution HAADF image from the selected area in Figure 6e. The nanoparticles with bright contrast bridge with each other to form a continuous structure; the bright area with the crystal lattice is assigned to cycled TiO_2 as marked by green dashed

lines, while the dark area with a disordered atomic arrangement is assigned to cycled SiO_x, which is marked by orange dashed lines. It is worth noting that residual lithium could exist in both phases. In high-resolution HAADF-EDX (Figure 6g), the Si and Ti signals show an inhomogeneous distribution, where the Si signal distribution is well-matched with the weak contrast area in the HAADF image, while the Ti signal distribution is associated with the bright area. Also, the Si/Ti color mix image shows an obvious wormlike Si signal distribution within the Ti signal distribution, proving the outstanding structural integrity even after 580 deep charge/discharge cycles. These results produce a sharp contrast with the mechanically mixed TiO_2/SiO_x without the mutual-stabilizing effect (Figure S15).

With the above *in situ/ex situ* characterizations on dynamic structure evolution and structural integrity, the long-term cycling stability of TiO_2/SiO_x can be tentatively attributed to the mutual-stabilizing effect, as illustrated in Figure 6h. In detail, the compact TiO_2/SiO_x composite enables consecutive electrochemical lithiation and delithiation, where the TiO_2 network is first lithiated (at a high potential) under the spatial confinement from the intimately packed SiO_x phase. At a low potential, the Li reacts with SiO_x, generating large volume expansion, which is, in the same way, confined and eased by the intimately packed lithiated TiO_2. The stress generated from one phase functions as the compressive force on the other phase and vice versa, offsetting the overall volume effect. The bicontinuous structure introduces abundant curvature-rich interfaces, which ease the stress accumulation. Meanwhile, reducing the size of compositing components to a sub 10 nm scale exponentially increases the intercomponent contact interfaces, further spreading the stress distribution. Moreover, the two interpenetrating phases with a large contact interface could interlock with each other, prohibiting the material loss and synergistically reinforcing the structural integrity during (de)lithiation. Their well-maintained small dimensional size as well as continuous nature would also facilitate the reaction kinetics and help releasing high capacity from both components. Through the mutual-stabilizing effect in the sub 10 nm scale, a large and stable capacity as well as a small volumetric change can be simultaneously realized. It should be mentioned that the concept of the mutual-stabilizing effect, in principle, could be applied to a wide class of high-capacity electrode materials through bicontinuous nanostructure design.

CONCLUSIONS

In this work, a sub 10 nm interfused bicontinuous TiO_2/SiO_x hybrid, in which bridged heterogeneous TiO_2 nanoparticles (over 80 wt %) are densely packed with the wormlike SiO_x network, is fabricated through a simple oxidation process of MAX Ti_3SiC_2 ceramic, utilizing its natural atomic Ti/Si dispersion distinction. When it is applied as the LIB anode material, the TiO_2/SiO_x hybrid exhibits a mutual-stabilizing effect, in which the two closely packed components would spatially confine and buffer each other's volume effect through lithiation. As a result, the TiO_2/SiO_x composite demonstrates a low volume change (~14%) and robust structural integrity even under an expanded electrochemical window of 0.01−3.0 V, enabling a high and stable lithium storage capability. This work presents a rational structure design with unraveled structure−property correlation, shedding light on the development of next-generation LIB anode materials with high capacity and longevity.

METHODS

Synthesis of TiO₂/SiOₓ Hybrid. The TiO_2/SiO_x hybrid was synthesized by processing commercial Ti_3SiC_2 MAX phase ceramic with a ball-milling procedure followed by one-step calcination in air. The Ti_3SiC_2 MAX phase ceramic was purchased from Guidechem (CAS 12202-82-3). The MAX ceramic was first processed with a ball-milling procedure where 2.0 g of the Ti_3SiC_2 was mixed with 24 stainless steel balls (20 steel balls with 6 mm diameter and 4 steel balls with 10 mm diameter) in a vial under an Ar atmosphere followed by a 2 h milling process at 300 rpm. The ball-milled Ti_3SiC_2 was then heated at 800 °C for 2 h with a heating rate of 10 °C min^{-1} in air. After it cooled to room temperature, the TiO_2/SiO_x hybrid was obtained.

Synthesis of Contrast Samples. The bare anatase TiO_2 nanoparticles were directly purchased from Aladdin (T104943). The Si nanoparticles were purchased from Aladdin (S130843), and q mechanically mixed TiO_2/Si mixture was prepared by ball-milling for 2 h at 300 rpm with an TiO_2/Si input mole ratio of 3/1. The mechanically mixed TiO_2/SiO_x was prepared by annealing the mechanically mixed TiO_2/Si mixture at 800 °C in air for 2 h.

Material Characterization. XRD characterizations were carried out on a D8 Discovery diffractometer (Bruker AXS, Karlsruhe, Germany). XRD patterns were recorded under the conditions of 40 mA tube current qand 40 kV tube voltage, and three graphs were recorded in a coupled 2θ mode for respectively 180 s. SEM images were collected using a JEOL-7100F scanning electron microscope. The TEM/STEM images, EELS/EDX spectra, and electron tomography experiments were collected using a CEOS probe corrected FEI Themis TEM instrument (electron accelerating voltage of 300 kV) equipped with a Gatan image filter spectrometer. The probe convergence angle was 17.8 mrad, and the probe current was ~45 pA for STEM imaging and EELS/EDS acquisition. EELS was performed with a Gatan Quantum 965 GIF system. Dual EELS was recorded for simultaneous visualization of zero loss and Ti M, Li K, and Ti L edges for calibration. The energy resolution was ~0.9 eV, which was determined by the full width at half-maximum of the zero-loss peak. Electron tomography experiments were performed on a Fischione tomography holder with a −80° to +80° tilt range. The reconstruction was performed using Thermo Fisher 3D Inspect and visualized in Avizo. *In situ* TEM was performed with a TEM-STM *in situ* sample holder (ZepTools Co. Ltd., China). *Ex situ* cross-sectional SEM images were collected by a FEI Helios Nanolab G3 dual beam focused ion beam, and the craters were sputtered by Ga$^+$. BET surface areas were measured with a Tristar II 3020 instrument with adsorption of nitrogen at 77 K. A TG analysis was carried out on a STA449c/3/G instrument (NETZSCH). XPS characterizations were carried out on a VG MultiLab 2000 instrument. Si L edge and Ti L edge XANES were tested at beamline U19 of the National Synchrotron Radiation Laboratory (NSRL, Hefei), in the total electron yield (TEY) mode with the sample drain current collected at under a vacuum of less than 10^{-7} Pa.

Electrochemical Characterization. The electrochemical properties were tested by assembling CR2016-type coin cells with lithium metal foil as the anode under an Ar atmosphere. The cathodes were composed of 70% active material, 10% sodium alginate binder, and 20% acetylene black. A solution (1.0 M) of $LiPF_6$ in ethyl carbonate/dimethyl carbonate/ethyl methyl carbonate (EC/DMC/EMC = 1/1/1 vol %) was used as the electrolyte. Copper foil was used as the collector. The mass loading of each electrode was 1.5−2.0 mg cm^{-2}. For the full cell, $LiFePO_4$ (LFP), PVDF, and acetylene black were mixed in a mass ratio of 8/1/1 to prepare the LFP cathode electrodes. The slurry was casted on an Al foil. The TiO_2/SiO_x hybrid anodes were prelithiated in half-cells and then assembled in the full cell. Cyclic voltammetry (0.01−3.0 V) was measured with a CHI 760S electrochemical workstation. Galvanostatic charge/discharge measurement was carried out on a multichannel battery testing system (LAND CT2001A). The *in situ* EIS was tested with a PGSTAT302N Autolab Potentiostat Galvanostat. The EIS was carried out on the same cell in the frequency range from 0.1 to 10000 Hz at open-circuit

potential before cycling and after the 1st, 5th, 20th, 25th, and 50th cycles. All of the measurements were carried out at room temperature. To prepare the sample after cycling for *ex situ* SEM and TEM characterization, the electrodes were taken out of the disassembled cell and then soaked in acetone for 48 h to remove the residual electrolyte.

ASSOCIATED CONTENT

ⓢ Supporting Information

The Supporting Information is available free of charge at https://pubs.acs.org/doi/10.1021/acsnano.2c10381.

> SEM images, TG analysis, N_2 adsorption−desorption isotherm, XRD patterns, and 3D reconstructed images of the TiO_2/SiO_x hybrids, *in situ* EIS profiles of the TiO_2/SiO_x hybrids, cycling performances of the TiO_2/SiO_x hybrids prepared at different calcination temperatures, structural characterization, cycling performances, and rate performances of bare anatase TiO_2 nanoparticles, mechanically mixed TiO_2/Si, and mechanically mixed TiO_2/SiO_x, electrochemical performances of various TiO_2-based anodes for LIBs and a comparison of retained capacities of various TiO_2-based anodes after cycling, charge−discharge curve and cycling perform-ance of the $TiO_2/SiO_x//LiFePO_4$ full cell, *ex situ* SEM images of the TiO_2/SiO_x hybrid electrode, and *ex situ* characterization of the structural degradation of mechanically mixed TiO_2/SiO_x after cycling (PDF)
>
> Rotation of the TiO_2/SiO_x hybrid from HAADF-STEM images at various tilt angles (MP4)
>
> Rotation, contrast segmentation, and orthoslicing process of the TiO_2/SiO_x hybrid from 3D reconstruction (MP4)
>
> Rotation and orthoslicing process of the inner volume of the TiO_2/SiO_x hybrid from 3D reconstruction (MP4)
>
> Rotation and orthoslicing process of TiO_2 and SiO_x components from contrast segmentation in 3D reconstruction (MP4)
>
> Place 1, *in situ* BF/HAADF-STEM characterization on lithiation of the TiO_2/SiO_x hybrid (MP4)
>
> Place 2, *in situ* BF/HAADF-STEM characterization on lithiation of the TiO_2/SiO_x hybrid (MP4)

AUTHOR INFORMATION

Corresponding Authors

Liang Zhou − *State Key Laboratory of Advanced Technology for Materials Synthesis and Processing, Wuhan University of Technology, Wuhan 430070, People's Republic of China; Hubei Longzhong Laboratory, Wuhan University of Technology (Xiangyang Demonstration Zone), Xiangyang 441000 Hubei, People's Republic of China;* ⓞ orcid.org/0000-0001-6756-3578; Email: liangzhou@whut.edu.cn

Jinsong Wu − *State Key Laboratory of Advanced Technology for Materials Synthesis and Processing, Wuhan University of Technology, Wuhan 430070, People's Republic of China; Nanostructure Research Centre, Wuhan University of Technology, Wuhan 430070, People's Republic of China;* ⓞ orcid.org/0000-0002-7305-7927; Email: wujs@whut.edu.cn

Liqiang Mai − *State Key Laboratory of Advanced Technology for Materials Synthesis and Processing, Wuhan University of Technology, Wuhan 430070, People's Republic of China; Hubei Longzhong Laboratory, Wuhan University of Technology (Xiangyang Demonstration Zone), Xiangyang 441000 Hubei, People's Republic of China;* ⓞ orcid.org/0000-0003-4259-7725; Email: mlq518@whut.edu.cn

Authors

Ruohan Yu − *State Key Laboratory of Advanced Technology for Materials Synthesis and Processing, Wuhan University of Technology, Wuhan 430070, People's Republic of China; Nanostructure Research Centre, Wuhan University of Technology, Wuhan 430070, People's Republic of China*

Yexin Pan − *Division of Integrative Systems and Design, The Hong Kong University of Science and Technology, Kowloon, Hong Kong SAR 999077, People's Republic of China*

Yihang Liu − *State Key Laboratory of Advanced Technology for Materials Synthesis and Processing, Wuhan University of Technology, Wuhan 430070, People's Republic of China*

Dongyuan Zhao − *State Key Laboratory of Advanced Technology for Materials Synthesis and Processing, Wuhan University of Technology, Wuhan 430070, People's Republic of China;* ⓞ orcid.org/0000-0001-8440-6902

Complete contact information is available at:
https://pubs.acs.org/10.1021/acsnano.2c10381

Author Contributions

The manuscript was written through contributions of all authors. All authors have given approval to the final version of the manuscript. R.Y., Y.P., and Y.L. contributed equally.

Notes

The authors declare no competing financial interest.

REFERENCES

(1) Meng, J.; Guo, H.; Niu, C.; Zhao, Y.; Xu, L.; Li, Q.; Mai, L. Advances in structure and property optimizations of battery electrode materials. *Joule* **2017**, *1* (3), 522−547.

(2) Liu, Y.; Zhu, Y.; Cui, Y. Challenges and opportunities towards fast-charging battery materials. *Nat. Energy* **2019**, *4* (7), 540−550.

(3) Zhu, G.-N.; Wang, Y.-G.; Xia, Y.-Y. Ti-based compounds as anode materials for Li-ion batteries. *Energy Environ. Sci.* **2012**, *5* (5), 6652−6667.

(4) Self, E. C.; Wycisk, R.; Pintauro, P. N. Electrospun titania-based fibers for high areal capacity Li-ion battery anodes. *J. Power Sources* **2015**, *282*, 187−193.

(5) Ren, Y.; Liu, Z.; Pourpoint, F.; Armstrong, A. R.; Grey, C. P.; Bruce, P. G. Nanoparticulate TiO_2 (B): an anode for lithium-ion batteries. *Angew. Chem., Int. Ed.* **2012**, *124* (9), 2206−2209.

(6) Zhang, W.; Seo, D.-H.; Chen, T.; Wu, L.; Topsakal, M.; Zhu, Y.; Lu, D.; Ceder, G.; Wang, F. Kinetic pathways of ionic transport in fast-charging lithium titanate. *Science* **2020**, *367* (6481), 1030−1034.

(7) Yang, L.; Luo, S.; Wang, Y.; Zhan, Y.; Wang, Q.; Zhang, Y.; Liu, X.; Mu, W.; Teng, F. Excess capacity on compound phases of Li_2FeTiO_4 composite cathode materials synthesized by hydrothermal reaction using optional titanium sources to boost battery perform-ance. *Chin. Chem. Lett.* **2020**, *31* (12), 3200−3204.

(8) Zhang, G.; Wu, H. B.; Song, T.; Paik, U.; Lou, X. W. TiO_2 hollow spheres composed of highly crystalline nanocrystals exhibit superior lithium storage properties. *Angew. Chem., Int. Ed.* **2014**, *53* (46), 12590−12593.

(9) Fang, Y.; Hu, R.; Liu, B.; Zhang, Y.; Zhu, K.; Yan, J.; Ye, K.; Cheng, K.; Wang, G.; Cao, D. MXene-derived TiO_2/reduced graphene oxide composite with an enhanced capacitive capacity for Li-ion and K-ion batteries. *J. Mater. Chem. A* **2019**, *7* (10), 5363−5372.

(10) He, R.; Liu, Z.; He, P.; Luo, W.; Yu, R.; Hong, X.; Pan, X.; Zhou, Q.; Mai, L.; Zhou, L. Constructing Three-Dimensional Macroporous TiO_2 Microspheres with enhanced pseudocapacitive lithium storage under deep discharging/charging conditions. *ACS Appl. Mater. Interfaces* **2021**, *13* (14), 16528−16535.

(11) Liu, Z.; Yu, Q.; Zhao, Y.; He, R.; Xu, M.; Feng, S.; Li, S.; Zhou, L.; Mai, L. Silicon oxides: a promising family of anode materials for lithium-ion batteries. *Chem. Soc. Rev.* **2019**, *48* (1), 285−309.

(12) Miyuki, T.; Okuyama, Y.; Sakamoto, T.; Eda, Y.; Kojima, T.; Sakai, T. Characterization of heat treated SiO powder and development of a $LiFePO_4$/SiO lithium ion battery with high-rate capability and thermostability. *Electrochemistry* **2012**, *80* (6), 401−404.

(13) Huang, X.; Guo, X.; Ding, Y.; Wei, R.; Mao, S.; Zhu, Y.; Bao, Z. Amorphous silicon from low-temperature reduction of silica in the molten salts and its lithium-storage performance. *Chin. Chem. Lett.* **2021**, *32* (2), 598−603.

(14) Wang, J.; Wang, X.; Liu, B.; Lu, H.; Chu, G.; Liu, J.; Guo, Y.-G.; Yu, X.; Luo, F.; Ren, Y.; et al. Size effect on the growth and pulverization behavior of Si nanodomains in SiO anode. *Nano Energy* **2020**, *78*, 105101.

(15) Kitada, K.; Pecher, O.; Magusin, P. C.; Groh, M. F.; Weatherup, R. S.; Grey, C. P. Unraveling the reaction mechanisms of SiO anodes for Li-ion batteries by combining in situ ^7Li and ex situ ^7Li/^{29}Si solid-state NMR spectroscopy. *J. Am. Chem. Soc.* **2019**, *141* (17), 7014−7027.

(16) Han, J.; Tang, D.-M.; Kong, D.; Chen, F.; Xiao, J.; Zhao, Z.; Pan, S.; Wu, S.; Yang, Q.-H. A thick yet dense silicon anode with enhanced interface stability in lithium storage evidenced by in situ TEM observations. *Sci. Bull.* **2020**, *65* (18), 1563−1569.

(17) Sun, L.; Xie, J.; Huang, S.; Liu, Y.; Zhang, L.; Wu, J.; Jin, Z. Rapid CO_2 exfoliation of Zintl phase $CaSi_2$-derived ultrathin free-standing Si/SiOx/C nanosheets for high-performance lithium storage. *Sci. China Mater.* **2022**, *65* (1), 51−58.

(18) Wang, L.; Xue, J.; Gao, B.; Gao, P.; Mou, C.; Li, J. Rice husk derived carbon-silica composites as anodes for lithium ion batteries. *RSC Adv.* **2014**, *4* (110), 64744−64746.

(19) Li, Z.; Zhao, H.; Lv, P.; Zhang, Z.; Zhang, Y.; Du, Z.; Teng, Y.; Zhao, L.; Zhu, Z. Watermelon-like structured SiO_x-TiO_2@ C nanocomposite as a high-performance lithium-ion battery anode. *Adv. Funct. Mater.* **2018**, *28* (31), 1605711.

(20) Yang, Z.; Ding, Y.; Jiang, Y.; Zhang, P.; Jin, H. Hierarchical C/SiO_x/TiO_2 ultrathin nanobelts as anode materials for advanced lithium ion batteries. *Nanotechnology* **2018**, *29* (40), 405602.

(21) Lee, G.; Kim, S.; Kim, S.; Choi, J. SiO_2/TiO_2 composite film for high capacity and excellent cycling stability in lithium-ion battery anodes. *Adv. Funct. Mater.* **2017**, *27* (39), 1703538.

(22) Singh, R.; Gupta, M.; Phase, D.; Mukherjee, S. Phase growth analysis of sputtered TiO_2 thin films at low oxygen partial pressures using XANES and XRR. *Mater. Res. Express.* **2019**, *6* (11), 116449.

(23) Tominaka, S.; Yoshikawa, H.; Matsushita, Y.; Cheetham, A. K. Topotactic reduction of oxide nanomaterials: unique structure and electronic properties of reduced TiO_2 nanoparticles. *Mater. Horizons* **2014**, *1* (1), 106−110.

(24) Liu, G.; Xu, L.; Li, Y.; Guo, D.; Wu, N.; Yuan, C.; Qin, A.; Cao, A.; Liu, X. Metal-organic frameworks derived anatase/rutile heterostructures with enhanced reaction kinetics for lithium and sodium storage. *Chem. Eng. J.* **2022**, *430*, 132689.

(25) Pinar Gokdemir, F.; Ece Yuzbasioglu, v.; Keskin, B.; Ozdemir, O.; Kutlu, K. Formation of TiO_2 thin films by a modified sol-gel route and characterization of structural, optical and electrochromic properties. *Adv. Mater. Lett.* **2014**, *5* (7), 367−371.

(26) Wang, J.; Wang, Z.; Wang, W.; Wang, Y.; Hu, X.; Liu, J.; Gong, X.; Miao, W.; Ding, L.; Li, X. Synthesis, modification and application of titanium dioxide nanoparticles: a review. *Nanoscale* **2022**, *14*, 6709−6734.

(27) Ren, Y.; Li, M. Facile synthesis of SiO_x@C composite nanorods as anodes for lithium ion batteries with excellent electrochemical performance. *J. Power Sources* **2016**, *306*, 459−466.

(28) Li, M.; Yu, Y.; Li, J.; Chen, B.; Wu, X.; Tian, Y.; Chen, P. Nanosilica/carbon composite spheres as anodes in Li-ion batteries with excellent cycle stability. *J. Mater. Chem. A* **2015**, *3* (4), 1476−1482.

(29) Li, M.; Zeng, Y.; Ren, Y.; Zeng, C.; Gu, J.; Feng, X.; He, H. Fabrication and lithium storage performance of sugar apple-shaped SiO_x@C nanocomposite spheres. *J. Power Sources* **2015**, *288*, 53−61.

(30) Choi, G.; Kim, J.; Kang, B. Understanding limited reversible capacity of a sio electrode during the first cycle and its effect on initial coulombic efficiency. *Chem. Mater.* **2019**, *31* (16), 6097−6104.

(31) Adhitama, E.; Dias Brandao, F.; Dienwiebel, I.; Bela, M. M.; Javed, A.; Haneke, L.; Stan, M. C.; Winter, M.; Gomez-Martin, A.; Placke, T. Pre-lithiation of silicon anodes by thermal evaporation of lithium for boosting the energy density of lithium ion cells. *Adv. Funct. Mater.* **2022**, *32*, 2201455.

(32) Zhang, C.; Siwu, L.; Jia, X. Research progress on the prelithiation technology of alloy-type anodes. *Energy Storage Science and Technology* **2022**, *11*, 1383−1400.

(33) Zhang, S.; Andreas, N. S.; Li, R.; Zhang, N.; Sun, C.; Lu, D.; Gao, T.; Chen, L.; Fan, X. Mitigating irreversible capacity loss for higher-energy lithium batteries. *Energy Stor. Mater.* **2022**, *48*, 44−73.

(34) Sun, J.; Zhang, S.; Zhang, Q.; Xin, Y.; Dong, S.; Liu, H.; Li, J.; Wang, C.; Lu, C.; Yang, W.; Liu, T.; Ma, J.; Gu, L.; Cui, G. Unshackling the reversible capacity of SiO_x/graphite-based full cells via selective LiF-induced lithiation. *Sci. China Mater.* **2022**, *65*, 2335−2342.

(35) Dong, H.; Wang, J.; Ding, H.; Wang, P.; Song, R.; Zhang, N.; Li, F.; Li, S. The mosaic structure design to improve the anchoring strength of SiO_x@C@graphite anode. *Mater. Today Chem.* **2021**, *22*, 100599.

(36) Tian, H.; Tian, H.; Yang, W.; Zhang, F.; Yang, W.; Zhang, Q.; Wang, Y.; Liu, J.; Silva, S. R. P.; Liu, H.; et al. Stable hollow-structured silicon suboxide-based anodes toward high-performance lithium-ion batteries. *Adv. Funct. Mater.* **2021**, *31* (25), 2101796.

(37) Zhang, J.; Hou, Z.; Zhang, X.; Zhang, L.; Li, C. Delicate construction of Si@SiO_x composite materials by microwave hydro-thermal for lithium-ion battery anodes. *Ionics* **2020**, *26* (1), 69−74.

(38) Cheng, X.; Li, Y.; Sang, L.; Ma, J.; Shi, H.; Liu, X.; Lu, J.; Zhang, Y. Boosting the electrochemical performance of MoO_3 anode for long-life lithium ion batteries: Dominated by an ultrathin TiO_2 passivation layer. *Electrochim. Acta* **2018**, *269*, 241−249.

(39) Li, F.; Li, J.; Zhu, F.; Liu, T.; Xu, B.; Kim, T.-H.; Kramer, M. J.; Ma, C.; Zhou, L.; Nan, C.-W. Atomically intimate contact between solid electrolytes and electrodes for Li batteries. *Matter* **2019**, *1* (4), 1001−1016.

(40) Jiang, N.; Spence, J. Core-hole effects on electron energy-loss spectroscopy of Li_2O. *Phys. Rev. B* **2004**, *69* (11), 115112.

(41) Lee, S.-Y.; Park, K.-Y.; Kim, W.-S.; Yoon, S.; Hong, S.-H.; Kang, K.; Kim, M. Unveiling origin of additional capacity of SnO_2 anode in lithium-ion batteries by realistic ex situ TEM analysis. *Nano Energy* **2016**, *19*, 234−245.

(42) Zhao, J.; Lee, H.-W.; Sun, J.; Yan, K.; Liu, Y.; Liu, W.; Lu, Z.; Lin, D.; Zhou, G.; Cui, Y. Metallurgically lithiated SiO_x anode with high capacity and ambient air compatibility. *Proc. Natl. Acad. Sci. U.S.A.* **2016**, *113* (27), 7408−7413.

(43) Gao, Q.; Gu, M.; Nie, A.; Mashayek, F.; Wang, C.; Odegard, G. M.; Shahbazian-Yassar, R. Direct evidence of lithium-induced atomic ordering in amorphous TiO_2 nanotubes. *Chem. Mater.* **2014**, *26* (4), 1660−1669.

(44) Su, Q.; Chang, L.; Zhang, J.; Du, G.; Xu, B. In situ TEM observation of the electrochemical process of individual CeO_2/graphene anode for lithium ion battery. *J. Phys. Chem. C* **2013**, *117* (8), 4292−4298.

(45) Lusvardi, V.; Barteau, M.; Chen, J. G.; Eng, J., Jr; Frühberger, B.; Teplyakov, A. An NEXAFS investigation of the reduction and reoxidation of TiO_2 (001). *Surf. Sci.* **1998**, *397* (1−3), 237−250.

(46) Akita, T.; Okumura, M.; Tanaka, K.; Ohkuma, K.; Kohyama, M.; Koyanagi, T.; Date, M.; Tsubota, S.; Haruta, M. Transmission electron microscopy observation of the structure of TiO2 nanotube and Au/TiO_2 nanotube catalyst. *Surf. Interface Anal.* **2005**, *37* (2), 265−269.

▢ Recommended by ACS

Templated Synthesis of SiO_2 Nanotubes for Lithium-Ion Battery Applications: An In Situ (Scanning) Transmission Electron Microscopy Study

Oskar Ronan, Valeria Nicolosi, *et al.*

DECEMBER 28, 2022
ACS OMEGA   READ ☑

Engineering High-Performance SiO_x Anode Materials with a Titanium Oxynitride Coating for Lithium-Ion Batteries

Guoyong Lai, Zhan Lin, *et al.*

OCTOBER 31, 2022
ACS APPLIED MATERIALS & INTERFACES   READ ☑

Silicon Nanospheres Supported on Conductive MXene Nanosheets as Anodes for Lithium-Ion Batteries

Hui Zhou, Xiaoming Zhang, *et al.*

DECEMBER 29, 2022
ACS APPLIED ENERGY MATERIALS   READ ☑

Constructing a Yolk–Shell Structure SiO_x/C@C Composite for Long-Life Lithium-Ion Batteries

Hang Luo, Yun Zhang, *et al.*

JULY 08, 2022
ACS APPLIED ENERGY MATERIALS   READ ☑

Get More Suggestions >